

# Hybrid WSe<sub>2</sub>–In<sub>2</sub>O<sub>3</sub> Phototransistor with Ultrahigh Detectivity by Efficient Suppression of Dark Currents

Nan Guo,<sup>†</sup> Fan Gong,<sup>‡,§</sup> Junku Liu,<sup>†</sup> Yi Jia,<sup>†</sup> Shaofan Zhao,<sup>†</sup> Lei Liao,<sup>§,||</sup> Meng Su,<sup>§</sup> Zhiyong Fan,<sup>||</sup> Xiaoshuang Chen,<sup>‡</sup> Wei Lu,<sup>‡</sup> Lin Xiao,<sup>\*,†</sup> and Weida Hu<sup>\*,‡,||</sup>

<sup>†</sup>Qian Xuesen Laboratory of Space Technology, China Academy of Space Technology, Beijing 100094, China

<sup>‡</sup>State Key Laboratory of Infrared Physics, Shanghai Institute of Technical Physics, Chinese Academy of Sciences, 500 Yutian Road, Shanghai 200083, China

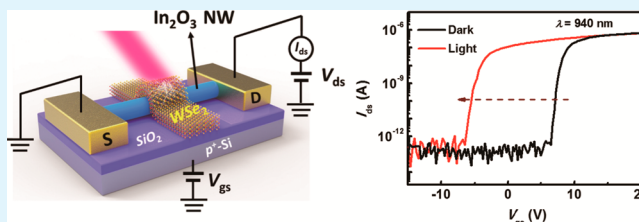
<sup>§</sup>Department of Physics and Key Laboratory of Artificial Micro- and Nano-Structures of Ministry of Education, Wuhan University, Wuhan 430072, China

<sup>||</sup>Department of Electronic and Computer Engineering, The Hong Kong University of Science and Technology, Clear Water Bay, Kowloon, Hong Kong, China

## Supporting Information

**ABSTRACT:** Photodetectors based on low-dimensional materials have attracted tremendous attention because of their high sensitivity and compatibility with conventional semiconductor technology. However, up until now, developing low-dimensional phototransistors with high responsivity and low dark currents over broad-band spectra still remains a great challenge because of the trade-offs in the potential architectures. In this work, we report a hybrid phototransistor consisting of a single In<sub>2</sub>O<sub>3</sub> nanowire as the channel material and a multilayer WSe<sub>2</sub> nanosheet as the decorating sensitizer for photodetection. Our devices show high responsivities of  $7.5 \times 10^5$  and  $3.5 \times 10^4$  A W<sup>-1</sup> and ultrahigh detectivities of  $4.17 \times 10^{17}$  and  $1.95 \times 10^{16}$  jones at the wavelengths of 637 and 940 nm, respectively. The superior detectivity of the hybrid architecture arises from the extremely low dark currents and the enhanced photogating effect in the depletion regime by the unique design of energy band alignment of the channel and sensitizer materials. Moreover, the visible to near-infrared absorption properties of the multilayer WSe<sub>2</sub> nanosheet favor a broad-band spectral response for the devices. Our results pave the way for developing ultrahigh-sensitivity photodetectors based on low-dimensional hybrid architectures.

**KEYWORDS:** nanowires, two-dimensional materials, hybrid structure, photogating effect, detectivity, responsivity



## INTRODUCTION

In recent years, emerging two-dimensional (2D) materials have shown great potential as high-performance photosensitive elements in future optoelectronic devices.<sup>1–21</sup> The unique properties of 2D materials, such as high charge carrier mobilities in graphene and thickness-dependent spectral coverage in transition-metal dichalcogenides, promise an extremely high gain-bandwidth and a wide spectral response for photodetection applications.<sup>14–16,22,23</sup> However, the inherent weak optical absorption of the atomic thickness nanomaterials leads to a low responsivity of photodetectors based on single 2D materials. For enhancing the light utilization efficiency, a promising strategy has been adopted to employ strongly light-absorbing materials with opposite doping polarity to decorate the channels.<sup>22–27</sup> The built-in field at the channel–sensitizer interface separates the photocarriers. The trapped carriers in the sensitizer lead to a photogating effect, which efficiently modulates the conductance of the channels to achieve a current amplification. An ultrahigh responsivity of  $\sim 10^7$  A W<sup>-1</sup> has been reported in hybrid graphene–quantum

dot (QD) phototransistors, where QDs and graphene act as the sensitizer and the channel, respectively.<sup>22</sup> However, the gapless graphene caused large dark currents, which result in a low sensitivity and high power consumptions. To address this issue, low-dimensional channel candidates with a band gap, such as MoS<sub>2</sub> and thin-film InGaZnO, are employed to deplete the dark currents by applying appropriate back-gate voltages.<sup>25–27</sup> Compared to graphene–QD phototransistors, several orders of magnitude reduction in dark currents have been demonstrated in the depletion regimes of MoS<sub>2</sub>–QD and InGaZnO–QD hybrid structures, but the corresponding photocurrents were simultaneously reduced to a relatively low level because of the alleviation of the built-in field by the back-gate electric field with the opposite direction. Therefore, despite tremendous efforts, it is still a great challenge for the low-dimensional

Received: July 21, 2017

Accepted: September 12, 2017

Published: September 12, 2017

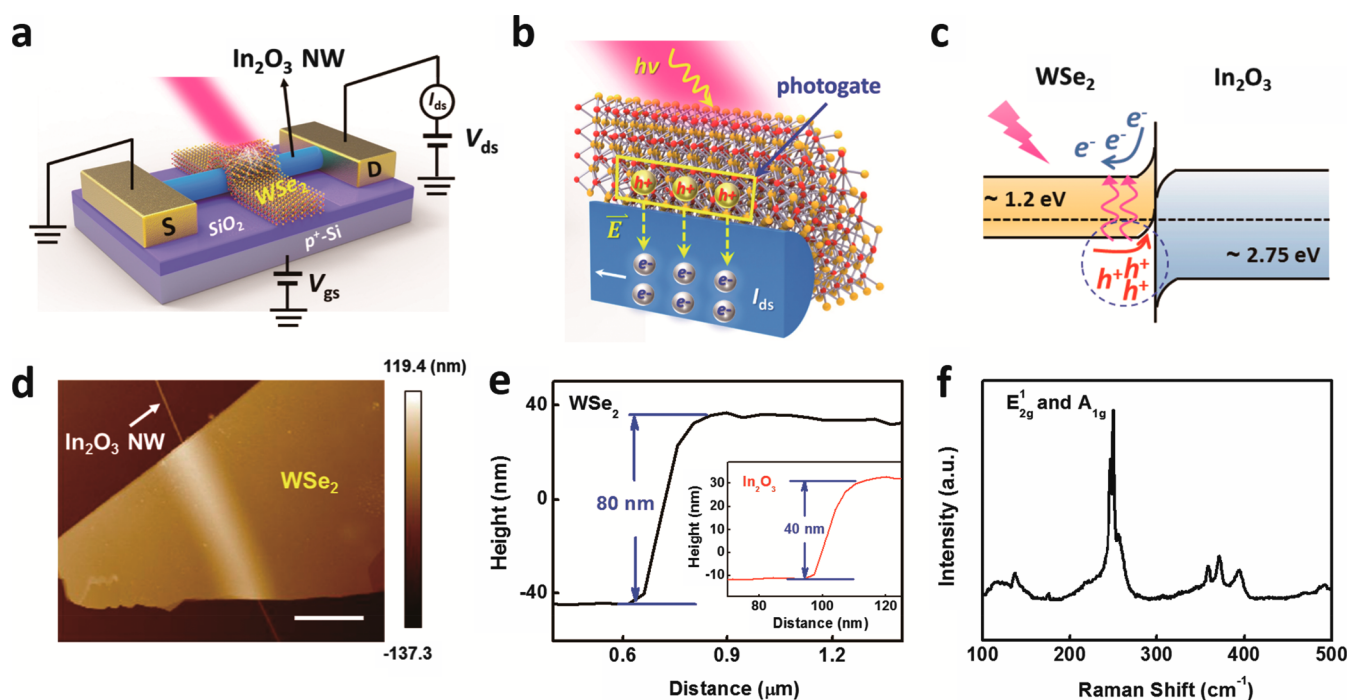


**Figure 1.** Multilayer WSe<sub>2</sub>–In<sub>2</sub>O<sub>3</sub> NW phototransistor. (a) Schematic illustration of the phototransistor, in which a multilayer WSe<sub>2</sub> is deposited onto a back-gated In<sub>2</sub>O<sub>3</sub> NW transistor. (b) Cross section of the device. The photoexcited holes in the WSe<sub>2</sub> are accumulated at the interface of the WSe<sub>2</sub> and the In<sub>2</sub>O<sub>3</sub> to modulate the NW conductance. (c) Energy band diagram at the junction formed by the WSe<sub>2</sub> and the In<sub>2</sub>O<sub>3</sub> NW. (d) AFM image of the hybrid structure (scale bar, 2 μm). (e) Height profiles of the WSe<sub>2</sub> (black line) and the In<sub>2</sub>O<sub>3</sub> NW (red line). (f) Raman spectrum of the multilayer WSe<sub>2</sub>.

phototransistors to operate at an optimized point with respect to the trade-off between responsivity and dark current.<sup>23</sup>

Here, we devise a multilayer WSe<sub>2</sub> nanosheet and In<sub>2</sub>O<sub>3</sub> nanowire (NW) hybrid structure for ultrahigh-sensitivity photodetection, where the WSe<sub>2</sub> serves as the sensitizer that modulates the channel NW conductance. Through the unique design of energy band alignment, the In<sub>2</sub>O<sub>3</sub> NW channel can be efficiently depleted with an external back-gate electric field, which meanwhile intensifies the strength of the built-in field at the WSe<sub>2</sub>–In<sub>2</sub>O<sub>3</sub> interface to ensure a stronger photogating effect. As a result, the phototransistor can be operated at extremely low dark currents (10<sup>−14</sup>–10<sup>−13</sup> A) and possesses a high photocurrent in the depletion regimes. Our devices show high responsivities of 7.5 × 10<sup>5</sup> and 3.5 × 10<sup>4</sup> A W<sup>−1</sup> and ultrahigh detectivities of 4.17 × 10<sup>17</sup> and 1.95 × 10<sup>16</sup> jones at the wavelengths of 637 and 940 nm, respectively. Additionally, because of the narrow band gap of the multilayer WSe<sub>2</sub>, the spectral response of the hybrid phototransistor covers the visible to near-infrared spectral range. Our experimental results pave the way for developing broad-band photodetectors with ultrahigh sensitivity based on low-dimensional hybrid architectures.

## RESULTS AND DISCUSSIONS

Figure 1a shows the multilayer WSe<sub>2</sub>–In<sub>2</sub>O<sub>3</sub> NW phototransistor configuration. The n-type In<sub>2</sub>O<sub>3</sub> NWs used in this work are grown by chemical vapor deposition (CVD) (see Methods). The device fabrication process can be briefly described as follows: First, In<sub>2</sub>O<sub>3</sub> NWs were physically transferred onto a Si/SiO<sub>2</sub> (100 nm) substrate. The source/drain (S/D) electrodes (15 nm Cr and 50 nm Au) were prepared by electron-beam lithography, metallization, and liftoff process. Then, a multilayer WSe<sub>2</sub> was transferred onto the

back-gated In<sub>2</sub>O<sub>3</sub> NW transistor by using a micromanipulator (see Methods). Figure S1 shows the transfer curves of the bare back-gated In<sub>2</sub>O<sub>3</sub> NW transistors. The devices present good electric properties. There is almost no hysteresis in the  $I_{ds}$ – $V_{gs}$  curves. The average mobility value is estimated to be 211 cm<sup>2</sup> V<sup>−1</sup> s<sup>−1</sup>.

The working principle of the hybrid phototransistor can be understood through the schematic and energy band diagram shown in Figure 1b,c, respectively. Figure S2 presents the band structures of the multilayer WSe<sub>2</sub> and the In<sub>2</sub>O<sub>3</sub> NW before they contact with each other. Because of the work function mismatch between the multilayer WSe<sub>2</sub> (band gap of ~1.2 eV)<sup>1,28–30</sup> and the In<sub>2</sub>O<sub>3</sub> NW (band gap of ~2.75 eV),<sup>31,32</sup> a built-in field is formed at the interface, leading to a band bending. As a result, the conduction/valence band edges of WSe<sub>2</sub> and In<sub>2</sub>O<sub>3</sub> NW bend upward and downward accordingly. In addition, a barrier is formed at the junction because of the big difference in electron affinity. Upon light exposure, when the photon energy is below the band gap of the In<sub>2</sub>O<sub>3</sub> NW but above that of the WSe<sub>2</sub>, the photocarriers are excited exclusively within the WSe<sub>2</sub>. The accumulated holes at the WSe<sub>2</sub>–In<sub>2</sub>O<sub>3</sub> interface generate a positive photogate to modulate the NW conductance through capacitive coupling, and a high responsivity can be obtained. To fully deplete the n-type In<sub>2</sub>O<sub>3</sub> NW channel, a back-gate voltage smaller than the threshold voltage is needed to apply on the phototransistor. The back-gate electric field with the same direction of the built-in field at the WSe<sub>2</sub>–In<sub>2</sub>O<sub>3</sub> interface intensifies the strength of the built-in field, leading to stronger band bending. The enhanced photogating effect in the depletion regime makes the detector operated at an extremely low dark current with high responsivity, resulting in a superior detectivity. Figure 1c shows the equilibrium band diagram of the WSe<sub>2</sub>–In<sub>2</sub>O<sub>3</sub> junction in

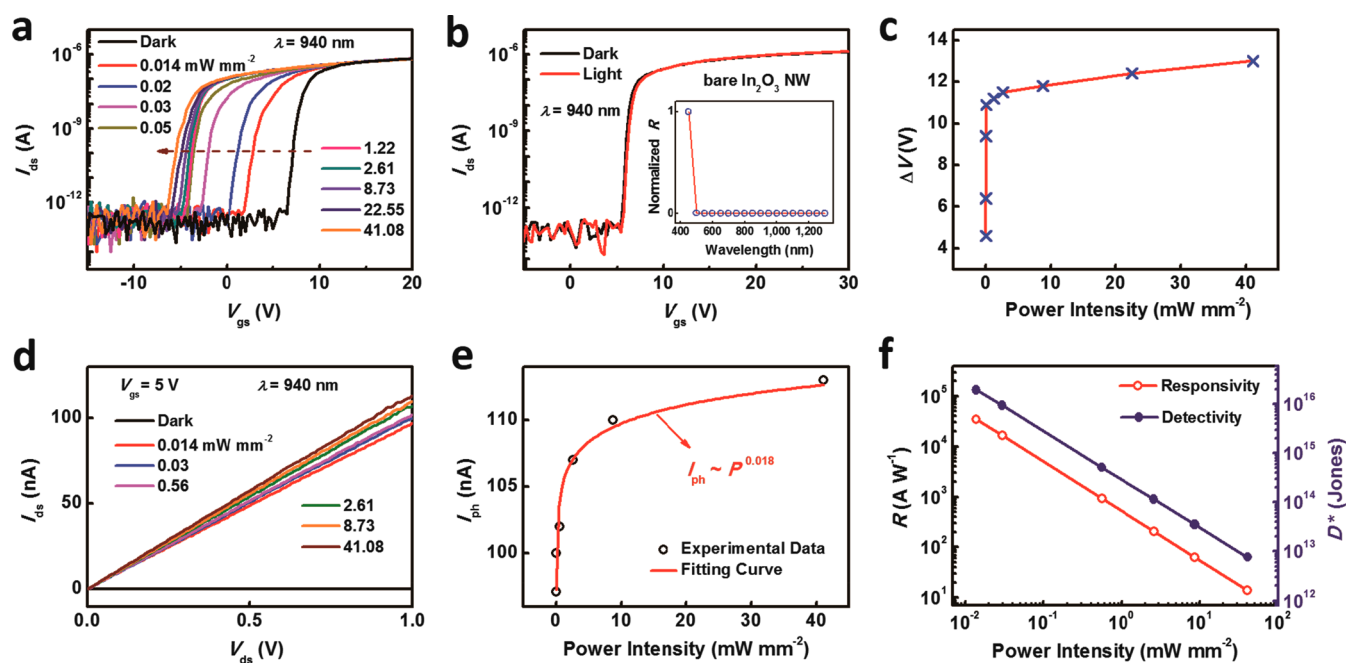


**Figure 2.** Photoresponse properties of the phototransistor. (a)  $I_{ds}$ - $V_{gs}$  curves of the phototransistor in the dark and under 940 nm illumination with different power intensities in air ( $V_{ds} = 1$  V). (b)  $I_{ds}$ - $V_{gs}$  curves of a bare  $\text{In}_2\text{O}_3$  NW transistor in the dark and under 940 nm illumination. The inset shows the normalized spectral responsivity of the bare  $\text{In}_2\text{O}_3$  NW transistor ( $V_{ds} = 1$  V). (c) Shift of threshold voltage as a function of light power intensity. (d)  $I_{ds}$ - $V_{ds}$  curves of the phototransistor in the dark and under 940 nm illumination with different power intensities in air. (e) Photocurrent as a function of light power intensity. (f) Responsivity and detectivity as a function of light power intensity.

the depletion regime, where the Fermi level of the n-type  $\text{In}_2\text{O}_3$  NW is close to the middle of band gap and that of the  $\text{WSe}_2$  is near the valence band edge because of the bipolar characteristic. It will be discussed in more detail later. Figure 1d,e shows an atomic force microscopy (AFM) image of the hybrid structure and the height profiles of the  $\text{WSe}_2$  and the  $\text{In}_2\text{O}_3$  NW, respectively. It can be seen that the NW height as measured from the uncovered portion is  $\sim 40$  nm and the height of the  $\text{WSe}_2$  is  $\sim 80$  nm. Figure S3a shows the 3D AFM image of the hybrid structure. The height profile of the overlapping area indicates that only the top of the  $\text{In}_2\text{O}_3$  NW contacts the  $\text{WSe}_2$  (see Figure S3b). Figure 1f presents the Raman spectrum of the  $\text{WSe}_2$ . The peaks at  $\sim 250$   $\text{cm}^{-1}$  correspond to the first-order  $E_{2g}$  and  $A_{1g}$  Raman modes, suggesting that the  $\text{WSe}_2$  has a multilayer morphology.<sup>33–35</sup> The thick  $\text{WSe}_2$  with a narrow band gap of  $\sim 1.2$  eV responds to the light wavelength from the visible to near-infrared range.

To investigate the photocurrent response for near-infrared range, the optoelectronic properties of the phototransistor under 940 nm light illumination were studied. Figure 2a presents the  $I_{ds}$ - $V_{gs}$  curves with different light power intensities in air. It is apparent that the light illumination causes a distinct negative shift of the threshold voltage, indicating that there is an additional positive photogate applied on the NW. Therefore, the device needs a more negative  $V_{gs}$  to offset the photogating effect. Moreover, the higher light intensity can excite more photocarriers in the  $\text{WSe}_2$ . The stronger photogate enhances the NW conductance, resulting in a larger negative threshold voltage (marked by a dashed arrow). It should be noted that, benefiting from the large band gap and efficient  $V_{gs}$  modulation of the channel material  $\text{In}_2\text{O}_3$  NW, the detector can operate at full depletion. Importantly, the band bending becomes more pronounced from the accumulation to depletion regimes by applying  $V_{gs}$ . More holes accumulated at the interface lead to an

efficient photogate. A high photocurrent ( $\sim 10^{-7}$  A) with an extremely low dark current ( $10^{-14}$ – $10^{-13}$  A) can be obtained in the depletion regime. This phenomenon will be explained below in detail. For comparison with the hybrid structure,  $I_{ds}$ - $V_{gs}$  properties of a bare  $\text{In}_2\text{O}_3$  NW transistor under 940 nm illumination are shown in Figure 2b. It can be seen that there is no obvious change in the currents. Furthermore, the inset of Figure 2b presents the normalized spectral responsivity of the bare  $\text{In}_2\text{O}_3$  NW transistor. No response can be observed when the photon energy is below the band gap of the  $\text{In}_2\text{O}_3$  NW (corresponding to a wavelength of 450 nm). Therefore, the photoresponse of the hybrid phototransistor for the near-infrared range is attributed to the multilayer  $\text{WSe}_2$ . The shift of threshold voltage ( $\Delta V$ ) as a function of power intensity is shown in Figure 2c. A rapid rise of  $\Delta V$  at low power intensity reveals the high photosensitivity of the hybrid phototransistor. Figure S4 shows the  $I_{ds}$ - $V_{gs}$  curves of another two samples with different areas of  $\text{WSe}_2$  in our work with a modulated 940 nm light illumination. The devices present good performance with a distinct photocurrent in the depletion regime and fast response. The average mobility value of the hybrid phototransistor is estimated to be  $143$   $\text{cm}^2$   $\text{V}^{-1}$   $\text{s}^{-1}$  under dark conditions.

Figure 2d depicts the  $I_{ds}$ - $V_{ds}$  characteristics of the phototransistor with different light power intensities. The fact that  $I_{ds}$  increases linearly with  $V_{ds}$  proves the good Ohmic contacts between the Cr/Au electrodes and the NW. Upon light exposure, a net photocurrent, defined as  $I_{pc} = I_{light} - I_{dark}$ , as high as  $\sim 113$  nA is obtained at  $V_{ds} = 1$  V. The relation between  $I_{pc}$  and light intensity ( $P$ ) obeys the power law  $I_{pc} \sim P^k$ , as shown in Figure 2e, where  $k$  is an empirical value.<sup>36–38</sup> By fitting the measured data with the equation,  $k = 0.018$  can be obtained. This relation further demonstrates that the accumulated photoexcited holes in the  $\text{WSe}_2$  are responsible for  $I_{pc}$ .

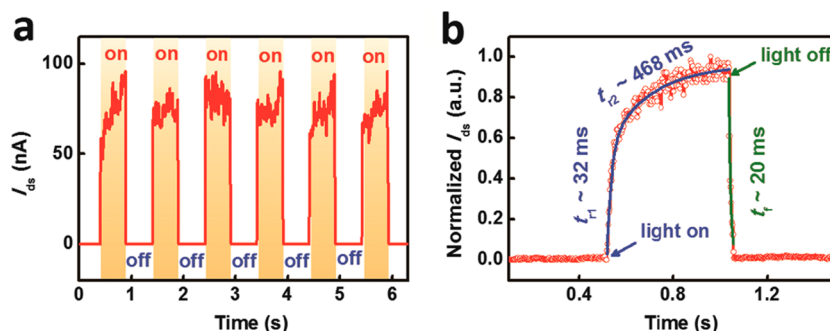


**Figure 3.** Temporal response characterization. (a) Temporal response of the phototransistor (940 nm) in air at  $V_{ds} = 1$  V. The light is turned on/off at an interval of 1 s. (b) Single modulation cycle (open circles). The blue and green lines indicate the rising and falling edges, respectively.

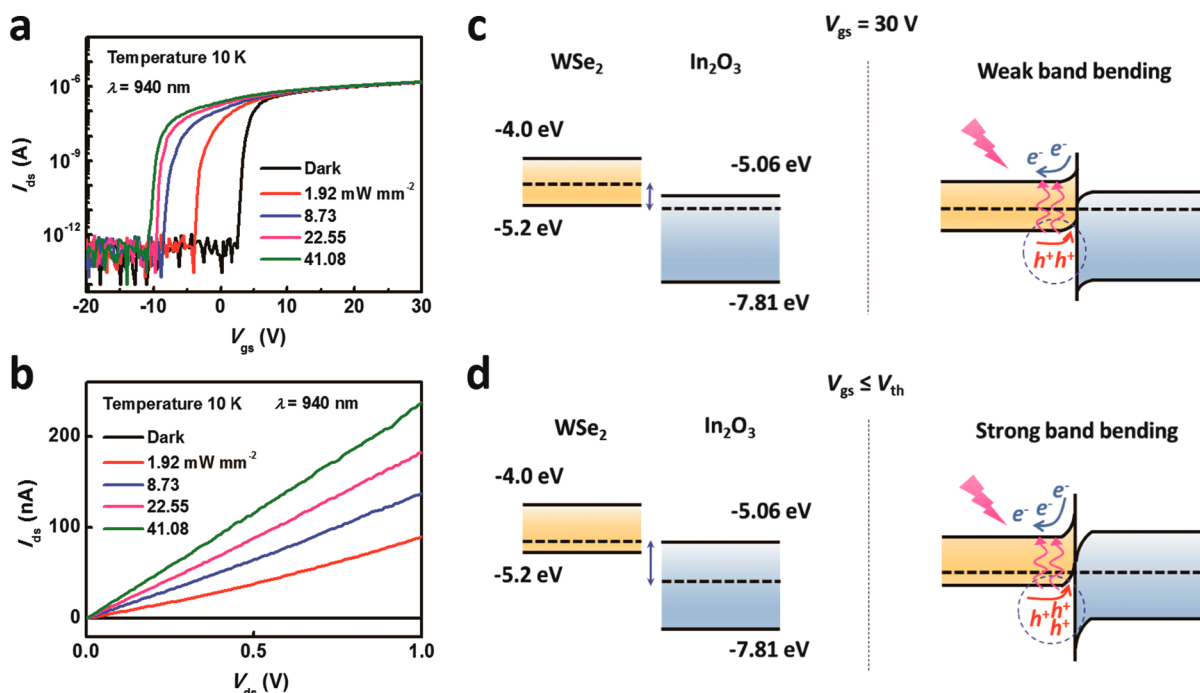


**Figure 4.** Photoresponse at low temperatures. (a)  $I_{ds}$ – $V_{gs}$  and (b)  $I_{ds}$ – $V_{ds}$  curves of the phototransistor in the dark and under 940 nm illumination with different power intensities at 10 K. (c) Energy band diagram at the junction formed by the  $\text{WSe}_2$  and the  $\text{In}_2\text{O}_3$  when the detector operated in the accumulation regime. (d) Energy band diagram at the junction formed by the  $\text{WSe}_2$  and the  $\text{In}_2\text{O}_3$  when the detector operated in the depletion regime.

Additionally, this  $I_{pc}$  saturation with the increase of light intensity may be due to the fact that no more photons can be absorbed by the  $\text{WSe}_2$  to excite excess carriers, which form a stronger electric field to enhance the NW conductance further. The responsivity ( $R$ ) as a function of light power intensity is shown in Figure 2f, given by  $R = I_{ph}/PA$ , where  $I_{ph}$  is the photocurrent,  $P$  is the power intensity, and  $A$  is the effective photoactive area.<sup>39–42</sup> In our case, the photoactive part is the overlapped area of the  $\text{WSe}_2$  and the  $\text{In}_2\text{O}_3$  NW. Under the assumption that light incident on the effective portion is absorbed completely, a responsivity of  $3.5 \times 10^4$   $\text{A W}^{-1}$  is obtained at  $V_{ds} = 1$  V. The specific detectivity as an important parameter to determine the capability of a photodetector to respond to a weak light signal is also shown in Figure 2f. Assuming that the shot noise from the dark current is a major contribution, the specific detectivity can be given as  $D^* = RA^{1/2}/(2eI_{dark})^{1/2}$ , where  $A$  is the effective photoactive area of the detector,  $e$  is the electron charge, and  $I_{dark}$  is the dark current.<sup>39,43</sup> This assumption is reasonable after the measure-

ment of noise current (see Figure S5 and the relative discussion in the Supporting Information). Because of the fact that the NW operates in an enhancement mode, in which the device has an off-current at  $V_{gs} = 0$  V and a positive threshold voltage, only a small gate bias can fully deplete the NW. Therefore, the extremely low  $I_{dark}$  results in a maximum  $D^*$  of  $1.95 \times 10^{16}$  jones ( $1 \text{ jones} = 1 \text{ cm Hz}^{1/2} \text{ W}^{-1}$ ). As expected, in our designed experiments, this high performance is ascribed to the efficient photogating effect in the depletion regime.

To further elucidate the physical mechanism of the phototransistor operation, response speed as a key figure of merit has been studied. The photoconductance modulation is realized by switching the incident light on and off periodically. As shown in Figure 3a, a high and a low current state under illuminated and dark conditions,  $I_{on}$  and  $I_{off}$  respectively, have been obtained with the light modulation. The switching between these two states exhibits highly stable and reversible characteristics. Figure 3b shows a single modulation cycle of temporal response. An oscilloscope was used to monitor the

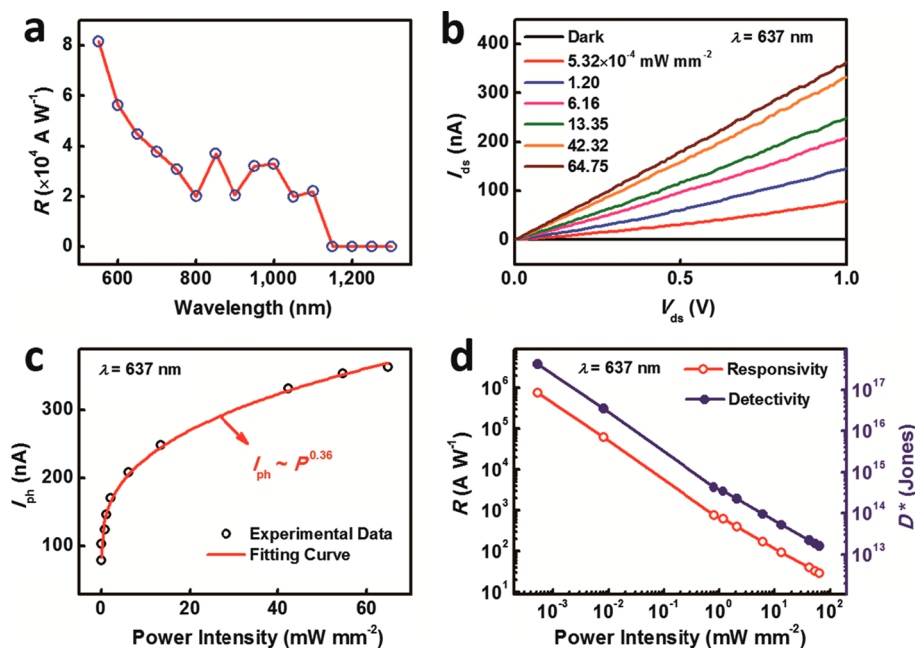


**Figure 5.** Wavelength dependence of photoresponse. (a) Spectral responsivity of the phototransistor. (b)  $I_{ds}$ – $V_{ds}$  curves of the phototransistor in the dark and under 637 nm illumination with different power intensities in air. (c) Photocurrent as a function of light power intensity. (d) Responsivity and detectivity as a function of light power intensity.

time dependence of the current. The rising edge, marked by a blue line, consists of a fast component for current increase from 0 to 60%  $I_{peak}$  ( $\sim 32$  ms) and a slow component for current increase from 60%  $I_{peak}$  to 100%  $I_{peak}$  ( $\sim 468$  ms). The former indicates the quick accumulation of photoexcited holes to form the photogate, and the latter indicates a little slow process to reach a stable state under light illumination. When the light was blocked, the current shows a sharp falling edge ( $\sim 20$  ms, green line), attributable to the rapid carrier recombination process. To testify that the response speed of the device mainly depends on that of the  $WSe_2$ , the temporal response of a bare back-gated multilayer  $WSe_2$  transistor under 940 nm illumination is shown in Figure S6a. The response and recovery time are at the level of  $\sim 20$  ms which is basically consistent with those of the  $WSe_2$ – $In_2O_3$  NW phototransistor. Moreover, the  $I$ – $V$  property and temporal response of the  $WSe_2$ – $In_2O_3$  heterostructure device under 940 nm light illumination are shown in Figure S7. No photoresponse is observed, proving that the photoexcited carriers in the  $WSe_2$  do not transfer to the  $In_2O_3$  NW to contribute photocurrents. Therefore, the  $WSe_2$  is believed to account for the response speed which can be improved if the photoactive material has an intrinsic fast process of carrier generation and recombination in the hybrid structure. Though earlier work on  $WSe_2$  phototransistors suggested that the response speed could be very fast ( $\sim 5$   $\mu s$ ),<sup>44</sup> the traps in the multilayer  $WSe_2$  in our case may be the reason for the restriction of the response speed. Moreover, it can also be seen in Figure S6a that the photocurrent is less than 2 nA and the dark current is hard to be suppressed by applying gate bias because of the bipolar behaviors (see Figure S6b). Compared with the performance of the hybrid phototransistor, the  $WSe_2$ -only photodetector is difficult to achieve high responsivity and detectivity under near-infrared light illumination with the same power intensity. Figure S8a,b and c,d shows the photoresponse properties of a bare  $In_2O_3$  NW transistor and a hybrid phototransistor under 405 nm light illumination, respectively.

The  $In_2O_3$  NW transistor displays a remarkable photocurrent but a slow response speed because of the persistent photoconductivity. The hybrid phototransistor shows the same performance. Therefore, when the photon energy is above the band gap of the  $In_2O_3$  NW, the photoresponse mainly originates from the  $In_2O_3$  NW.

To investigate the photoresponse of the device at low temperatures, the optoelectronic properties under 940 nm light illumination were studied at 10 K. Figure 4a presents the  $I_{ds}$ – $V_{gs}$  curves with different power intensities. The light illumination also leads to a distinct negative shift of  $V_{th}$ . With an increase of intensity,  $V_{th}$  moves toward a larger negative  $V_{gs}$ , which is the same as the measured results at room temperature. Figure 4b depicts the  $I_{ds}$ – $V_{ds}$  characteristics with different power intensities. The photocurrents at 10 K are higher than those obtained at room temperature (see Figure 2d) under the same illumination conditions. This is because of the suppression of electron–phonon scattering at the low temperature, resulting in a higher mobility of the  $In_2O_3$  NW. Under the light illumination, the photogate modulates the NW conductance and the carriers in the NW can be collected faster by the S/D electrodes to form a high  $I_{ds}$ . Additionally, the low temperature provides a condition to study the effect of back gate on the strength of photogate well without thermal influence. Figure S9a shows the linear curves of Figure 4a. It is obvious that a larger photocurrent can be acquired in the depletion regime in comparison with that in the accumulation regime. Figure 4c,d shows the corresponding band alignments at these two operating conditions. Under  $V_{gs} = 30$  V, the position of Fermi level in the multilayer  $WSe_2$  is located close to the middle of band gap because of the charge neutral point at around 37 V (see Figure S6b). In addition, the position of Fermi level in the  $In_2O_3$  NW is near the conduction band edge because of the n-type property. The little difference in work function (see the double-headed arrow in Figure 4c) leads to a small band bending. Less photoexcited holes accumulate at the

Table 1. Optoelectronic Characteristics of Typical Hybrid Phototransistors

| material   | dark current in operating point (A)  | wavelength (nm)                     | responsivity (A W <sup>-1</sup> )              | detectivity (jones)                                | recovery time | references |
|--|--------------------------------------|-------------------------------------|--|--|---------------|------------|
| graphene-QD  | 10 <sup>-6</sup>                     | visible<br>near-infrared            | ~10 <sup>7</sup><br>~10 <sup>5</sup>           | 7 × 10 <sup>13</sup>                               | 1 s           | 22         |
| graphene-carbon nanotube   | 10 <sup>-6</sup>                     | 650                                 | >100   |  | ~100 μs       | 24         |
| MoS <sub>2</sub> -QD   | 10 <sup>-7</sup>                     | 1500<br>400–1000                    | >10<br>>10 <sup>5</sup>                        | 10 <sup>11</sup>                                   | 0.3–0.4 s     | 25         |
| MoS <sub>2</sub> -TiO <sub>2</sub> -QD   | 10 <sup>-11</sup>                    | 635<br>1000–1500                    | 10 <sup>3</sup><br>~10 <sup>4</sup>            | 10 <sup>12</sup>                                   | 12 ms         | 26         |
| InGaZnO-QD   | 10 <sup>-5</sup>                     | 1000                                | 10 <sup>6</sup>                                | 10 <sup>13</sup>                                   | 0.2–0.3 s     | 27         |
| graphene-perovskite  |                                      | 520                                 | 180  | 10 <sup>9</sup>                                    | 540 ms        | 45         |
| WSe <sub>2</sub> -QD   | 2.5 × 10 <sup>-7</sup>               | 970                                 | 2 × 10 <sup>5</sup>                            | 7 × 10 <sup>13</sup>                               | 0.48 s        | 46         |
| WS <sub>2</sub> -Bi <sub>2</sub> Te <sub>3</sub>                                 |                                      | 370–1550                            | 30.4   | 2.3 × 10 <sup>11</sup>                             | 20 ms         | 47         |
| In <sub>2</sub> O <sub>3</sub> -In <sub>2</sub> (TeO <sub>3</sub> ) <sub>3</sub> |                                      | 370–635                             | 0.18   | 5.3 × 10 <sup>9</sup>                              |               | 48         |
| WSe <sub>2</sub> -In <sub>2</sub> O <sub>3</sub> NW                              | 10 <sup>-14</sup> –10 <sup>-13</sup> | visible<br>near-infrared (500–1100) | 7.5 × 10 <sup>5</sup><br>3.5 × 10 <sup>4</sup> | 4.17 × 10 <sup>17</sup><br>1.95 × 10 <sup>16</sup> | 20 ms         | this work  |

interface to generate a weak photogate, resulting in a small photocurrent. Oppositely, under  $V_{gs} \leq V_{th}$ , the position of Fermi level in the WSe<sub>2</sub> is near the valence band edge and that in the In<sub>2</sub>O<sub>3</sub> NW is located close to the middle of band gap. The big difference in work function (see the double-headed arrow in Figure 4d) leads to a large band bending. More holes accumulate at the interface to generate a strong photogate, resulting in a large photocurrent. This is the advantage in our design that the band bending becomes more pronounced from the accumulation to depletion regimes. Finally, the device can be operated at extremely low dark currents with high photoresponse. The optoelectronic properties at 77 K under 940 nm light illumination are shown in Figure S9b,c. The hybrid phototransistor presents the same performance in comparison with that measured at 10 K.

Because of the narrow band gap of the multilayer WSe<sub>2</sub>, the hybrid phototransistor is expected to work from the visible to near-infrared range. Properties of broad-band response of the device are investigated by using a monochromator. To avoid the response of the In<sub>2</sub>O<sub>3</sub> NW, the wavelength ( $\lambda$ ) is varied from 550 to 1300 nm with an interval of 50 nm. During measurement, the light intensity for different  $\lambda$  values kept consistent at 0.014 mW mm<sup>-2</sup>. Figure S10a presents the partial data of the  $I_{ds}$ - $V_{gs}$  characteristics with different  $\lambda$  values in air (another device in our work). It is obvious that the phototransistor responds to the light from the visible to near-infrared range and a high photon energy causes a more negative  $V_{th}$ .  $\Delta V$  increases with the decrease of  $\lambda$ , which is because of the fact that the incident photons with a high energy will excite the photocarriers in the WSe<sub>2</sub> more efficiently to form a stronger photogate (see Figure S10b). The spectral responsivities of the device are shown in Figure 5a. With  $\lambda$  changing from visible to near-infrared, the responsivity decreases by more than half from 550 to 750 nm. Then, it remains relatively steady from 750 nm to 1.1 μm. No response can be observed when  $\lambda$  is beyond 1.1 μm. It is worth noting that the band gap of the multilayer WSe<sub>2</sub> is ~1.2 eV, corresponding to  $\lambda$  of ~1 μm. In addition, the bare In<sub>2</sub>O<sub>3</sub> NW device does not respond to 1.1 μm light (the inset of Figure 2b). Therefore, the extending cutoff wavelength may be ascribed to the defects in the WSe<sub>2</sub>. To further testify that the broad-band response of the phototransistor originates from the WSe<sub>2</sub>, the spectral responsivity of a bare multilayer WSe<sub>2</sub> photodetector is shown in Figure S11. Clearly, compared with

the large photocurrent in the visible range, a smaller photocurrent is obtained in the near-infrared range up to 1.1 μm. This demonstrates that only a few photocarriers generated in the WSe<sub>2</sub> can induce a high photoresponse in the hybrid structure.

To investigate the photocurrent response for the visible-light range, the optoelectronic properties of the device under 637 nm illumination were studied. Figure 5b depicts the  $I_{ds}$ - $V_{ds}$  characteristics with different light power intensities. A net photocurrent  $I_{pc}$  as high as ~364 nA is obtained at  $V_{ds} = 1$  V. Because of the high photon energy, a lower light intensity can induce a larger photocurrent in comparison with that show in Figure 2d. The relation between  $I_{pc}$  and light intensity also obeys the power law  $I_{pc} \sim P^k$  (see Figure 5c). By fitting the measured data with the equation,  $k = 0.36$  can be obtained. The maximum  $R$  of  $7.5 \times 10^5$  A W<sup>-1</sup> and  $D^*$  of  $4.17 \times 10^{17}$  jones at  $V_{ds} = 1$  V are 1 order of magnitude larger than those measured under 940 nm illumination (see Figure 5d). Table 1 summarizes the reported detectors with high responsivity in the visible and near-infrared range. Obviously, the device in our work has extremely low dark current, ultrahigh  $D^*$ , comparable  $R$ , and relatively fast response speed under the same operating condition.

## CONCLUSIONS

In summary, we have demonstrated a simple 2D material and one-dimensional NW hybrid architecture to possess a broad-band photoresponse with high performance. The devices exhibit ultrahigh detectivity because of an enhanced photogating effect in the depletion regime, where extremely low dark currents and relatively high responsivity can be simultaneously achieved. By decoupling the absorption from the charge transport with independent materials, the phototransistors can respond to a wide spectral range from visible to near-infrared because of the absorption properties of the multilayer WSe<sub>2</sub> nanosheet. Our study shows a successful endeavor to optimize the dark currents and responsivity for hybrid low-dimensional phototransistors by the unique design of energy band alignment of the channel and sensitizer materials. The simple architecture also ensures a great flexibility for the realization of high-performance photodetectors in other spectral ranges, such as mid-wavelength infrared and long-

wavelength infrared, by appropriate choices of desired band gap sensitizers and transport channels.

## METHODS

**NW Growth.** In<sub>2</sub>O<sub>3</sub> NWs used in this study were prepared by a CVD method. In<sub>2</sub>O<sub>3</sub> powder and graphite powder were mixed at a weight ratio of 10:1 and then put into a quartz boat. A silicon substrate with predeposition of 1 nm thick Au catalyst was placed upside down atop the quartz boat. Then, the entire setup was inserted into a tube reactor, heated to 1050 °C, and kept at this temperature for 1 h under a constant flow of gas (argon/oxygen = 100:1; 200 sccm). Finally, the substrate was cooled to room temperature naturally.

**Phototransistor Fabrication and Characterization.** The WSe<sub>2</sub> nanosheets were mechanically exfoliated on a Si/SiO<sub>2</sub> (285 nm) substrate. A thin layer of water-soluble polyvinyl acetate (PVA) was adhered to poly(dimethylsiloxane) (PDMS) to pick up the WSe<sub>2</sub> nanosheets. A micromanipulator was used to put the PDMS/PVA layer onto certain targets by using a microscope to locate the position. First, the PDMS/PVA layer picked up a WSe<sub>2</sub> nanosheet from the substrate. Then, the WSe<sub>2</sub> nanosheet was precisely aligned to the target back-gated In<sub>2</sub>O<sub>3</sub> NW transistor to form the hybrid structure. The PVA release from PDMS was performed through heating to soften the PVA layer. Finally, PVA was removed from the hybrid structure in deionized water. The optoelectronic properties of the phototransistors were characterized using a Lake Shore probe station together with an Agilent B1500 semiconductor parameter analyzer. The spectral responsivity was analyzed using a supercontinuum spectrum laser source (400–2400 nm) combined with a monochromator and an Agilent B2902.

## ASSOCIATED CONTENT

### Supporting Information

The Supporting Information is available free of charge on the ACS Publications website at DOI: 10.1021/acsami.7b10698.

Transfer curves of bare In<sub>2</sub>O<sub>3</sub> NW transistors; band structure of the multilayer WSe<sub>2</sub> and In<sub>2</sub>O<sub>3</sub> NW; 3D AFM image of the hybrid phototransistor; noise current measurement; temporal response of a bare back-gated multilayer WSe<sub>2</sub> transistor; photoresponse properties of the WSe<sub>2</sub>–In<sub>2</sub>O<sub>3</sub> heterostructure device; photoresponse properties of a bare In<sub>2</sub>O<sub>3</sub> NW transistor and a hybrid phototransistor under 405 nm illumination; photoresponse properties of the hybrid phototransistor at 77 K; and spectral responsivity of a bare back-gated multilayer WSe<sub>2</sub> transistor (PDF)

## AUTHOR INFORMATION

### Corresponding Authors

\*E-mail: xiaolin@qxslab.cn (L.X.).

\*E-mail: wdhu@mail.sitp.ac.cn (W.H.).

### ORCID

Lei Liao: 0000-0003-1325-2410

Zhiyong Fan: 0000-0002-5397-0129

Weida Hu: 0000-0001-5278-8969

### Author Contributions

N.G., L.X., and W.H. conceived and supervised the research. N.G., F.G., and S.Z. fabricated the devices. N.G. and J.L. performed the measurements. L.L. and M.S. performed the NW growth. N.G., Z.F., L.X., and W.H. wrote the paper. All authors discussed the results and revised the manuscript.

### Notes

The authors declare no competing financial interest.

## ACKNOWLEDGMENTS

This work was partially supported by the Natural Science Foundation of China (grant nos. 11734016, 11334008, 51502337, 61674157, and 51472019), Key Research Project of Frontier Science of CAS (grant no. QYZDB-SSW-JSC031), Open Research Fund Program of the State Key Laboratory of Infrared Physics, Royal Society-Newton Advanced Fellowship, Open Research Fund Program of the State Key Laboratory of Low-Dimensional Quantum Physics, the Center for 1D/2D Quantum Materials, and the State Key Laboratory on Advanced Displays and Optoelectronics at HKUST.

## REFERENCES

- (1) Wang, Q. H.; Kalantar-Zadeh, K.; Kis, A.; Coleman, J. N.; Strano, M. S. Electronics and Optoelectronics of Two-Dimensional Transition Metal Dichalcogenides. *Nat. Nanotechnol.* **2012**, *7*, 699–712.
- (2) Baugher, B. W. H.; Churchill, H. O. H.; Yang, Y.; Jarillo-Herrero, P. Optoelectronic Devices Based on Electrically Tunable P–N Diodes in a Monolayer Dichalcogenide. *Nat. Nanotechnol.* **2014**, *9*, 262–267.
- (3) Massicotte, M.; Schmidt, P.; Violla, F.; Schädler, K. G.; Reserbat-Plantey, A.; Watanabe, K.; Taniguchi, T.; Tielrooij, K. J.; Koppens, F. H. L. Picosecond Photoresponse in van Der Waals Heterostructures. *Nat. Nanotechnol.* **2016**, *11*, 42–46.
- (4) Long, M.; Liu, E.; Wang, P.; Gao, A.; Xia, H.; Luo, W.; Wang, B.; Zeng, J.; Fu, Y.; Xu, K.; Zhou, W.; Lv, Y.; Yao, S.; Lu, M.; Chen, Y.; Ni, Z.; You, Y.; Zhang, X.; Qin, S.; Shi, Y.; Hu, W.; Xing, D.; Miao, F. Broadband Photovoltaic Detectors Based on an Atomically Thin Heterostructure. *Nano Lett.* **2016**, *16*, 2254–2259.
- (5) Yu, W. J.; Liu, Y.; Zhou, H.; Yin, A.; Li, Z.; Huang, Y.; Duan, X. Highly Efficient Gate-Tunable Photocurrent Generation in Vertical Heterostructures of Layered Materials. *Nat. Nanotechnol.* **2013**, *8*, 952–958.
- (6) Jo, S.-H.; Kang, D.-H.; Shim, J.; Jeon, J.; Jeon, M. H.; Yoo, G.; Kim, J.; Lee, J.; Yeom, G. Y.; Lee, S.; Yu, H.-Y.; Choi, C.; Park, J.-H. A High-Performance WSe<sub>2</sub>/H-BN Photodetector Using a Triphenylphosphine (PPh<sub>3</sub>)-Based N-Doping Technique. *Adv. Mater.* **2016**, *28*, 4824–4831.
- (7) Kang, D.-H.; Kim, M.-S.; Shim, J.; Jeon, J.; Park, H.-Y.; Jung, W.-S.; Yu, H.-Y.; Pang, C.-H.; Lee, S.; Park, J.-H. High-Performance Transition Metal Dichalcogenide Photodetectors Enhanced by Self-Assembled Monolayer Doping. *Adv. Funct. Mater.* **2015**, *25*, 4219–4227.
- (8) Zhang, W.; Chiu, M.-H.; Chen, C.-H.; Chen, W.; Li, L.-J.; Wee, A. T. S. Role of Metal Contacts in High-Performance Phototransistors Based on WSe<sub>2</sub> Monolayers. *ACS Nano* **2014**, *8*, 8653–8661.
- (9) Lopez-Sanchez, O.; Lembke, D.; Kayci, M.; Radenovic, A.; Kis, A. Ultrasensitive Photodetectors Based on Monolayer MoS<sub>2</sub>. *Nat. Nanotechnol.* **2013**, *8*, 497–501.
- (10) Pospischil, A.; Humer, M.; Furchi, M. M.; Bachmann, D.; Guider, R.; Fromherz, T.; Mueller, T. CMOS-Compatible Graphene Photodetector Covering All Optical Communication Bands. *Nat. Photonics* **2013**, *7*, 892–896.
- (11) Gabor, N. M.; Song, J. C. W.; Ma, Q.; Nair, N. L.; Taychatanapat, T.; Watanabe, K.; Taniguchi, T.; Levitov, L. S.; Jarillo-Herrero, P. Hot Carrier-Assisted Intrinsic Photoresponse in Graphene. *Science* **2011**, *334*, 648–652.
- (12) Liu, C.-H.; Chang, Y.-C.; Norris, T. B.; Zhong, Z. Graphene Photodetectors with Ultra-Broadband and High Responsivity at Room Temperature. *Nat. Nanotechnol.* **2014**, *9*, 273–278.
- (13) Liu, N.; Tian, H.; Schwartz, G.; Tok, J. B.-H.; Ren, T.-L.; Bao, Z. Large-Area, Transparent, and Flexible Infrared Photodetector Fabricated Using P-N Junctions Formed by N-Doping Chemical Vapor Deposition Grown Graphene. *Nano Lett.* **2014**, *14*, 3702–3708.
- (14) Liu, M.; Yin, X.; Ulin-Avila, E.; Geng, B.; Zentgraf, T.; Ju, L.; Wang, F.; Zhang, X. A Graphene-Based Broadband Optical Modulator. *Nature* **2011**, *474*, 64–67.

- (15) Mueller, T.; Xia, F.; Avouris, P. Graphene Photodetectors for High-Speed Optical Communications. *Nat. Photonics* **2010**, *4*, 297–301.
- (16) Wang, X.; Wang, P.; Wang, J.; Hu, W.; Zhou, X.; Guo, N.; Huang, H.; Sun, S.; Shen, H.; Lin, T.; Tang, M.; Liao, L.; Jiang, A.; Sun, J.; Meng, X.; Chen, X.; Lu, W.; Chu, J. Ultrasensitive and Broadband MoS<sub>2</sub> Photodetector Driven by Ferroelectrics. *Adv. Mater.* **2015**, *27*, 6575–6581.
- (17) Yao, J.; Zheng, Z.; Yang, G. All-Layered 2D Optoelectronics: A High-Performance UV–vis–NIR Broadband SnSe Photodetector with Bi<sub>2</sub>Te<sub>3</sub> Topological Insulator Electrodes. *Adv. Funct. Mater.* **2017**, *27*, 1701823.
- (18) Yao, J.; Zheng, Z.; Shao, J.; Yang, G. Promoting Photosensitivity and Detectivity of the Bi/Si Heterojunction Photodetector by Inserting a WS<sub>2</sub> Layer. *ACS Appl. Mater. Interfaces* **2015**, *7*, 26701–26708.
- (19) Yao, J.; Zheng, Z.; Yang, G. Promoting the Performance of Layered-Material Photodetectors by Alloy Engineering. *ACS Appl. Mater. Interfaces* **2016**, *8*, 12915–12924.
- (20) Yao, J. D.; Zheng, Z. Q.; Shao, J. M.; Yang, G. W. Stable, Highly-Responsive and Broadband Photodetection Based on Large-Area Multilayered WS<sub>2</sub> Films Grown by Pulsed-Laser Deposition. *Nanoscale* **2015**, *7*, 14974–14981.
- (21) Yao, J.; Shao, J.; Wang, Y.; Zhao, Z.; Yang, G. Ultra-Broadband and High Response of the Bi<sub>2</sub>Te<sub>3</sub>–Si Heterojunction and Its Application as a Photodetector at Room Temperature in Harsh Working Environments. *Nanoscale* **2015**, *7*, 12535–12541.
- (22) Konstantatos, G.; Badioli, M.; Gaudreau, L.; Osmond, J.; Bernechea, M.; de Arquer, F. P. G.; Gatti, F.; Koppens, F. H. L. Hybrid Graphene-Quantum Dot Phototransistors with Ultrahigh Gain. *Nat. Nanotechnol.* **2012**, *7*, 363–368.
- (23) Kufer, D.; Konstantatos, G. Photo-FETs: Phototransistors Enabled by 2D and 0D Nanomaterials. *ACS Photonics* **2016**, *3*, 2197–2210.
- (24) Liu, Y.; Wang, F.; Wang, X.; Wang, X.; Flahaut, E.; Liu, X.; Li, Y.; Wang, X.; Xu, Y.; Shi, Y.; Zhang, R. Planar Carbon Nanotube–graphene Hybrid Films for High-Performance Broadband Photodetectors. *Nat. Commun.* **2015**, *6*, 8589.
- (25) Kufer, D.; Nikitskiy, I.; Lasanta, T.; Navickaite, G.; Koppens, F. H. L.; Konstantatos, G. Hybrid 2D–0D MoS<sub>2</sub>–PbS Quantum Dot Photodetectors. *Adv. Mater.* **2015**, *27*, 176–180.
- (26) Kufer, D.; Lasanta, T.; Bernechea, M.; Koppens, F. H. L.; Konstantatos, G. Interface Engineering in Hybrid Quantum Dot–2D Phototransistors. *ACS Photonics* **2016**, *3*, 1324–1330.
- (27) Hwang, D. K.; Lee, Y. T.; Lee, H. S.; Lee, Y. J.; Shokouh, S. H.; Kyhm, J.-H.; Lee, J.; Kim, H. H.; Yoo, T.-H.; Nam, S. H.; Son, D. I.; Ju, B.-K.; Park, M.-C.; Song, J. D.; Choi, W. K.; Im, S. Ultrasensitive PbS Quantum-Dot-Sensitized InGaZnO Hybrid Photoinverter for near-Infrared Detection and Imaging with High Photogain. *NPG Asia Mater.* **2016**, *8*, No. e233.
- (28) Kumar, A.; Ahluwalia, P. K. Electronic Structure of Transition Metal Dichalcogenides Monolayers 1H-MX<sub>2</sub> (M = Mo, W; X = S, Se, Te) from Ab-Initio Theory: New Direct Band Gap Semiconductors. *Eur. Phys. J. B* **2012**, *85*, 186.
- (29) Chen, P.; Zhang, T. T.; Zhang, J.; Xiang, J.; Yu, H.; Wu, S.; Lu, X.; Wang, G.; Wen, F.; Liu, Z.; Yang, R.; Shi, D.; Zhang, G. Gate Tunable WSe<sub>2</sub>–BP van Der Waals Heterojunction Devices. *Nanoscale* **2016**, *8*, 3254–3258.
- (30) Lei, B.; Hu, Z.; Xiang, D.; Wang, J.; Eda, G.; Han, C.; Chen, W. Significantly Enhanced Optoelectronic Performance of Tungsten Diselenide Phototransistor via Surface Functionalization. *Nano Res.* **2017**, *10*, 1282–1291.
- (31) Scanlon, D. O.; Regoutz, A.; Egdel, R. G.; Morgan, D. J.; Watson, G. W. Band Gap Engineering of In<sub>2</sub>O<sub>3</sub> by Alloying with Ti<sub>2</sub>O<sub>3</sub>. *Appl. Phys. Lett.* **2013**, *103*, 262108.
- (32) Pan, C. A.; Ma, T. P. Work Function of In<sub>2</sub>O<sub>3</sub> Film as Determined from Internal Photoemission. *Appl. Phys. Lett.* **1980**, *37*, 714–716.
- (33) Lin, Y.-C.; Chang, C.-Y. S.; Ghosh, R. K.; Li, J.; Zhu, H.; Addou, R.; Diaconescu, B.; Ohta, T.; Peng, X.; Lu, N.; Kim, M. J.; Robinson, J. T.; Wallace, R. M.; Mayer, T. S.; Datta, S.; Li, L.-J.; Robinson, J. A. Atomically Thin Heterostructures Based on Single-Layer Tungsten Diselenide and Graphene. *Nano Lett.* **2014**, *14*, 6936–6941.
- (34) Fan, J.-H.; Gao, P.; Zhang, A. M.; Zhu, B. R.; Zeng, H. L.; Cui, X. D.; He, R.; Zhang, Q. M. Resonance Raman Scattering in Bulk 2H-MX<sub>2</sub> (M = Mo, W; X = S, Se) and Monolayer MoS<sub>2</sub>. *J. Appl. Phys.* **2014**, *115*, 053527.
- (35) Yu, X.; Prévot, M. S.; Guijarro, N.; Sivula, K. Self-Assembled 2D WSe<sub>2</sub> Thin Films for Photoelectrochemical Hydrogen Production. *Nat. Commun.* **2015**, *6*, 7596.
- (36) Kung, S.-C.; van der Veer, W. E.; Yang, F.; Donovan, K. C.; Penner, R. M. 20 μs Photocurrent Response from Lithographically Patterned Nanocrystalline Cadmium Selenide Nanowires. *Nano Lett.* **2010**, *10*, 1481–1485.
- (37) Wu, P.; Dai, Y.; Ye, Y.; Yin, Y.; Dai, L. Fast-Speed and High-Gain Photodetectors of Individual Single Crystalline Zn<sub>3</sub>P<sub>2</sub> Nanowires. *J. Mater. Chem.* **2011**, *21*, 2563–2567.
- (38) Jiang, Y.; Zhang, W. J.; Jie, J. S.; Meng, X. M.; Fan, X.; Lee, S.-T. Photoresponse Properties of CdSe Single-Nanoribbon Photodetectors. *Adv. Funct. Mater.* **2007**, *17*, 1795–1800.
- (39) Liu, X.; Gu, L.; Zhang, Q.; Wu, J.; Long, Y.; Fan, Z. All-Printable Band-Edge Modulated ZnO Nanowire Photodetectors with Ultra-High Detectivity. *Nat. Commun.* **2014**, *5*, 4007.
- (40) Guo, Y.; Yu, G.; Liu, Y. Functional Organic Field-Effect Transistors. *Adv. Mater.* **2010**, *22*, 4427–4447.
- (41) Konstantatos, G.; Sargent, E. H. Nanostructured Materials for Photon Detection. *Nat. Nanotechnol.* **2010**, *5*, 391–400.
- (42) Li, L.; Gu, L.; Lou, Z.; Fan, Z.; Shen, G. ZnO Quantum Dot Decorated Zn<sub>2</sub>SnO<sub>4</sub> Nanowire Heterojunction Photodetectors with Drastic Performance Enhancement and Flexible Ultraviolet Image Sensors. *ACS Nano* **2017**, *11*, 4067–4076.
- (43) Gong, X.; Tong, M.; Xia, Y.; Cai, W.; Moon, J. S.; Cao, Y.; Yu, G.; Shieh, C.-L.; Nilsson, B.; Heeger, A. J. High-Detectivity Polymer Photodetectors with Spectral Response from 300 nm to 1450 nm. *Science* **2009**, *325*, 1665–1667.
- (44) Pradhan, N. R.; Ludwig, J.; Lu, Z.; Rhodes, D.; Bishop, M. M.; Thirunavukkuarasu, K.; McGill, S. A.; Smirnov, D.; Balicas, L. High Photoresponsivity and Short Photoresponse Times in Few-Layered WSe<sub>2</sub> Transistors. *ACS Appl. Mater. Interfaces* **2015**, *7*, 12080–12088.
- (45) Lee, Y.; Kwon, J.; Hwang, E.; Ra, C.-H.; Yoo, W. J.; Ahn, J.-H.; Park, J. H.; Cho, J. H. High-Performance Perovskite–Graphene Hybrid Photodetector. *Adv. Mater.* **2015**, *27*, 41–46.
- (46) Hu, C.; Dong, D.; Yang, X.; Qiao, K.; Yang, D.; Deng, H.; Yuan, S.; Khan, J.; Lan, Y.; Song, H.; Tang, J. Synergistic Effect of Hybrid PbS Quantum Dots/2D-WSe<sub>2</sub> Toward High Performance and Broadband Phototransistors. *Adv. Funct. Mater.* **2017**, *27*, 1603605.
- (47) Yao, J.; Zheng, Z.; Yang, G. Layered-Material WS<sub>2</sub>/Topological Insulator Bi<sub>2</sub>Te<sub>3</sub> Heterostructure Photodetector with Ultrahigh Responsivity in the Range from 370 to 1550 nm. *J. Mater. Chem. C* **2016**, *4*, 7831–7840.
- (48) Yao, J.; Zheng, Z.; Yang, G. An Innovative Postdeposition Annealing Approach Producing Centimeter-Scale In<sub>2</sub>O<sub>3</sub>/In<sub>2</sub>(TeO<sub>3</sub>)<sub>3</sub> Bulk Heterojunction Thin Film for Room-Temperature Persistent Photoconductivity. *Adv. Opt. Mater.* **2017**, *5*, 1600908.